Supporting Information for

Rational Design and Mechanical Understanding of Three-Dimensional Macro-/Mesoporous Silicon Lithium-Ion Battery Anodes with Tunable Pore size and Wall Thickness

Xiuxia Zuo[†a], Yi Wen[†*b], Yike Qiu[†c], Ya-Jun Cheng[*a, d], Shanshan Yin[a, e], Qing Ji[a, f], Zhong You[g], Jin Zhu[a], Peter Müller-Buschbaum[e, h], Lifeng Ma*[c], Peter G Bruce[d, i, j], and Yonggao Xia[*a, k]

[a.] Ningbo Institute of Materials Technology & Engineering, Chinese Academy of Sciences, 1219 Zhongguan West Rd, Ningbo, 315201, Zhejiang Province, P. R. China

[b.] National Demonstration Center for Experimental Mechanics Education, School of Aerospace, Xi'an Jiaotong University, 28 Xianning West Rd, Xi'an 710049, Shaanxi Province, P. R. China

[c.] Department of engineering mechanics, Xi'an Jiaotong University, 28 Xianning West Rd, Xi'an 710049, Shaanxi Province, P. R. China

[d.] Department of Materials, University of Oxford, Parks Rd, OX1 3PH, Oxford, UK

[e.] Physik-Department, Lehrstuhl für Funtionelle Materielien, Technische Universität München, James-Franck-Strasse 1, 85748 Garching, Germany

[f.] The University of Nottingham Ningbo China,199 Taikang East Road, Ningbo, 315100, Zhejiang Province, P. R. China

[g.] Department of Engineering Science, Parks Road, University of Oxford, Oxford, OX1 3PJ, U.K.

[h.] Heinz Maier-Leibnitz Zentrum (MLZ), Technische Universität München, Lichtenbergstr. 1, 85748 Garching, Germany

[i.] The Henry Royce Institute, Parks Road, Oxford, OX1 3PH, UK

[j.] The Faraday Institution, Quad One, Becquerel Avenue, Harwell Campus, Didcot, OX11 0RA, UK

[k.] Center of Materials Science and Optoelectronics Engineering， University of Chinese Academy of Sciences, 19A Yuquan Rd, Shijingshan District, Beijing 100049, P. R. China

[*]Corresponding author.

Email address: wenyi@mail.xjtu.edu.cn, chengyj@nimte.ac.cn, xiayg@nimte.ac.cn,

malf@mail.xjtu.edu.cn

[†]X.Z., Y.Wen., and Y.Q. contribute equally to this work.

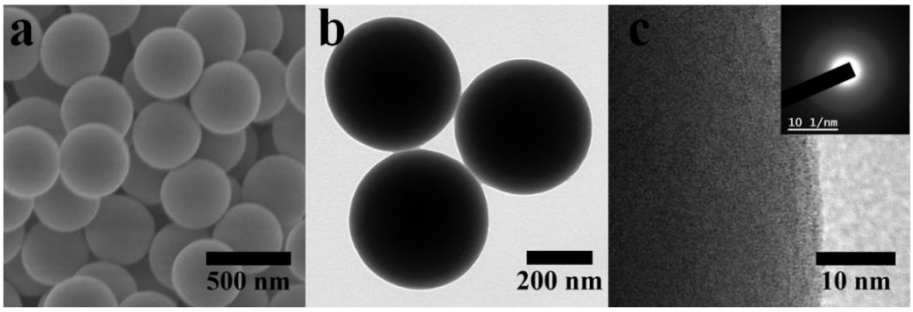

Figure S1. (a) SEM, (b) TEM, and (c) HRTEM images (inset: SAED pattern) of the pristine SiO_2.

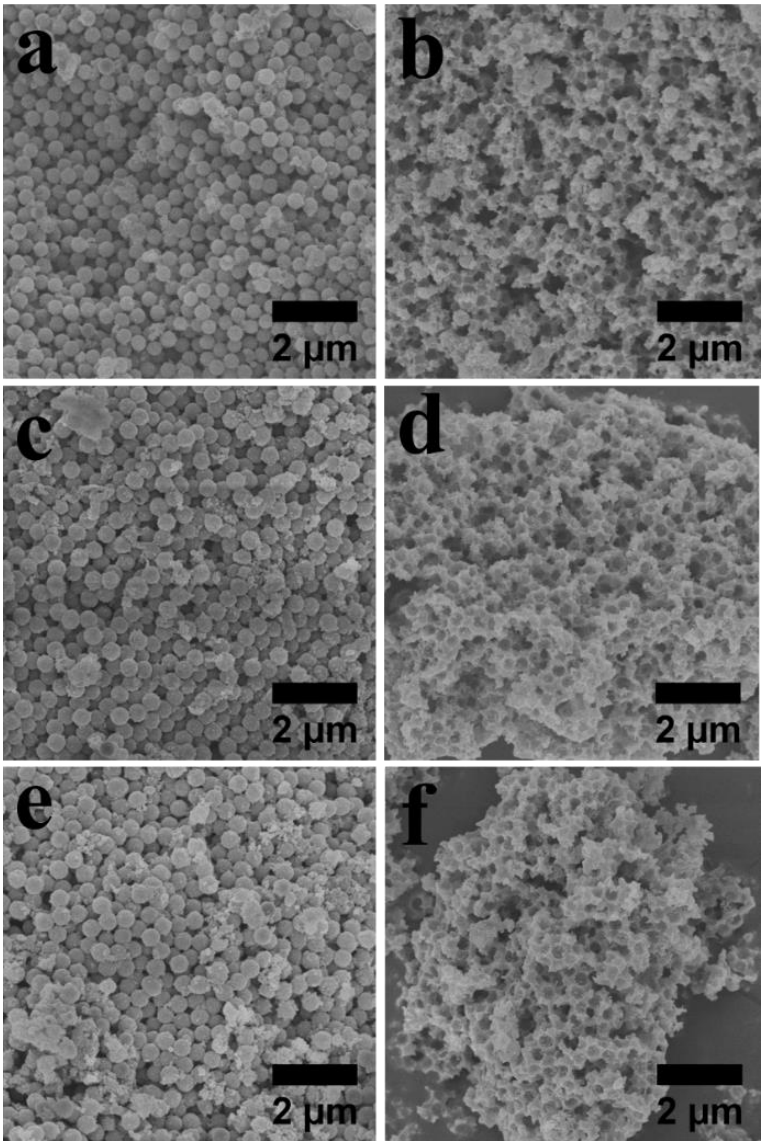

Figure S2.SEM images of porous silicon samples. (a) HCl-4h, (b) HF-4h, (c) HCl-8h, (d) HF-8h, (e) HCl-16h, and (f) HF-16h.

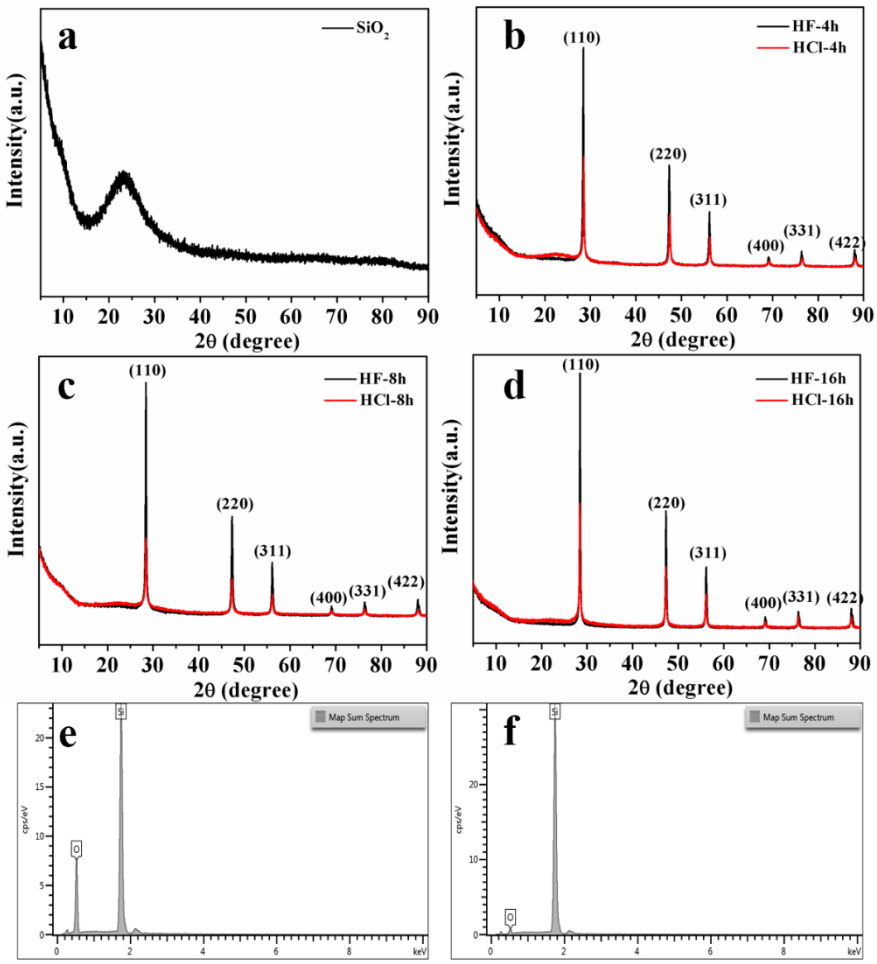

Figure S3. XRD patterns of (a) pristine SiO_2, (b) HCl-4h and HF-4h, (c) HCl-8h and HF-8h, (d) HCl-16h and HF-16h; EDS of (e) HCl-16h and (f) HF-16h

Figure S3 compares the XRD patterns of as-prepared SiO_2 and the samples obtained after different magnesiothermic reduction times, followed by a post treatment. As shown in Figure S3a, pristine SiO_2 has a typical amorphous structure with a weak broad diffraction peak located at approximately 23 °. After magnesiothermic reduction, six characteristic diffraction peaks are present at 28.4 °, 47.3 °, 56.1 °, 69.1 °, 76.4 ° and 86.0 °, which can be well assigned to the (111), (220), (311), (400), (331) and (422) crystal planes of the cubic phase of Si (JCPDS 27-1402). Thus, it confirms that Si has been successfully synthesized with the reduction time ranging from 4 h to 16 h. However, the broad diffraction peak located at around 23 ° is observed for the HCl-4h sample, which is invisible in the samples with a reduction time of 8 h and 16 h. It indicates that the extended reaction time converts more silica into silicon. With HF treatment, all of the samples still show almost identical diffraction patterns belonging to crystalline silicon. Particularly,

the weak broad peak from the amorphous silica in the HCl-4h sample disappears after the HF treatment. It suggests that HF has effectively removed the un-reacted silica. The EDS patterns in Figure S3e and S3f show that the intensity of the oxygen peak for HF-16h is significantly decreased compared with HCl-16h, indicating removal of the residual silica. The weak oxygen peak existing in the HF-16h sample is related to the oxide layer on the surface of the porous silicon.

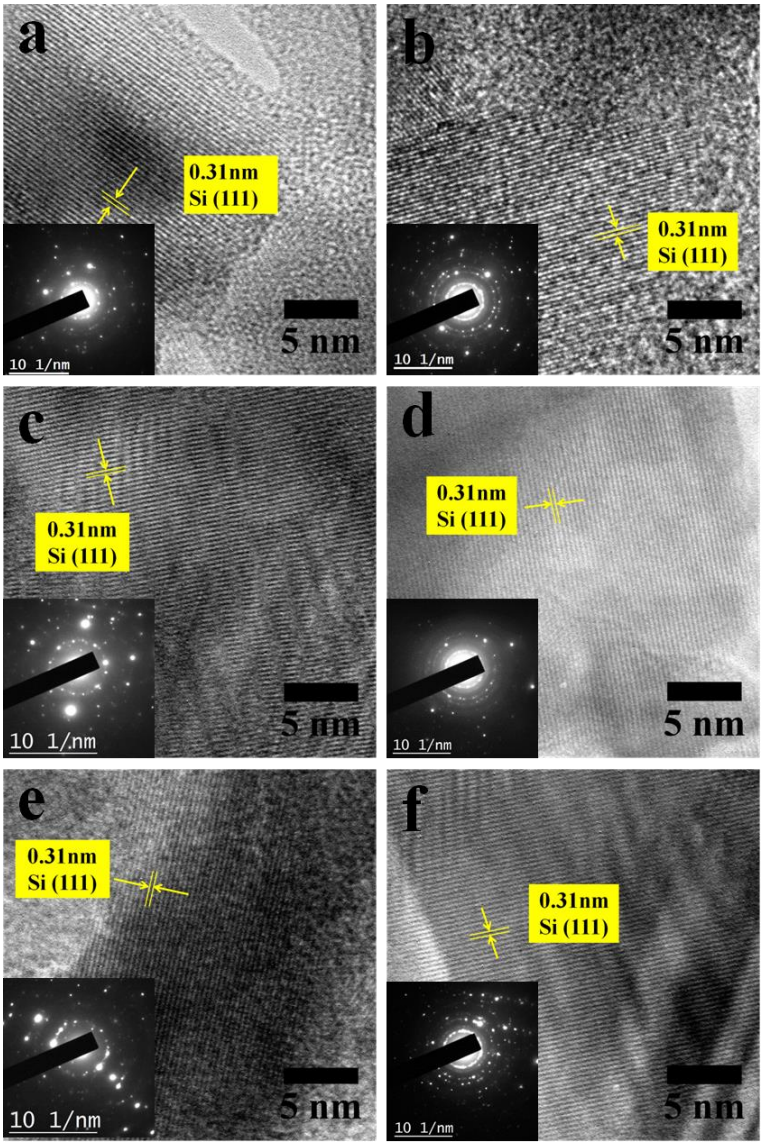

Figure S4. HRTEM images and SAED patterns (inset of each image) of porous silicon. (a) HCl-4h, (b) HF-4h, (c) HCl-8h, (d) HF-8h, (e) HCl-16h, and (f) HF-16h.

The high resolution TEM (HRTEM) combined with the SAED patterns in **Figure S4** confirms that the magnesiothermic reduction time applied in this work is sufficient to yield crystalline silicon under 700 °C. The d-spacing of 0.31 nm corresponds to the distance between neighboring (111) planes of the cubic phase of silicon, which agrees well with the XRD profiles. Considering that both the HCl washing and HF etching treatments themselves unlikely modify crystallinity of the local silicon, it is reasonable to conclude that crystallized silicon observed in the HRTEM images originate from the reduction process.

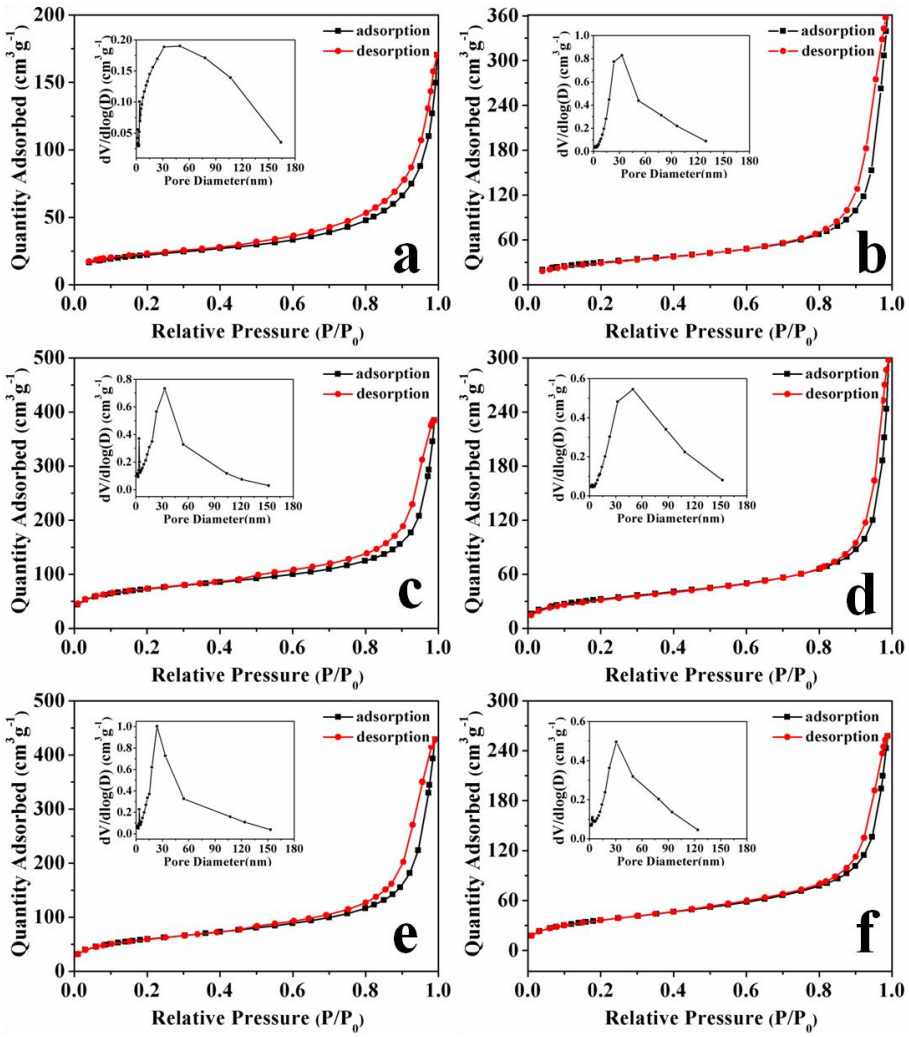

Figure S5. N_2 adsorption and desorption isotherms and corresponding BJH pore size distribution curves (inset of each image) of porous silicon. (a) HCl-4h, (b) HF-4h, (c) HCl-8h, (d) HF-8h, (e) HCl-16h, and (f) HF-16h.

Porosity information including pore size distribution, specific surface area, and pore volume of the HCl-washing samples and HF-etching silicon is obtained. As shown in **Figure S5**, the N_2 adsorption/desorption isotherms of all six samples display a characteristic type-IV isotherm with a H_3 hysteresis loop at the range of 0.8 P/P_0 - 1.0 P/P_0, which suggests the existence of mesoporous structures. The pore size distribution profile of the HCl-washing samples derived from the BJH method is broad in case of a reduction time of 4 h. It is narrowed with the reduction time being extended to 8 h and 16 h. The peak positions shift gradually to smaller sizes with increased reduction time (40 nm, 33 nm, and 24 nm, respectively). Unlike the pore size obtained with the BJH method, the average pore diameter calculated

with the equation of 4V/A (A: BET specific surface area, V: pore volume) does not show a clear trend, being in the mesoscopic range between 10 nm and 21 nm. The BET surface areas of the HCl-washing samples increase gradually along for increasing reduction time (which are 79.2 m^2g^{-1}, 215.1 m^2g^{-1}, and 257.5 m^2g^{-1}, respectively see Table 1). Both the SEM and TEM images of the HCl-washing samples prove that the silica particles react with magnesium. Particularly, the TEM images display mesopores within the silica particles, which make significant contributions to high specific surface area. Therefore, the relatively small specific surface area of the HCl-4h sample likely originates from limited reaction between silica and magnesium due to short reduction time (4 h vs. 8 h and 16 h). Besides the specific surface area, the pore volume also gradually increases with longer reduction times (from 4 h to 8 h and 16 h). The corresponding values are 0.26 cm^3g^{-1}, 0.56 cm^3g^{-1}, and 0.64 cm^3g^{-1}, respectively. These findings are consistent with the change of the specific surface area, which is also due to enhanced reduction of the silica particles by the magnesium. In details, the extent of the increased specific surface area and pore volume with the reduction time from 4 h to 8 h is much larger than with the reduction time from 8 h to 16 h. It suggests that the reduction of the silica particles is significantly promoted with the reduction time from 4 h to 8 h. Finally, the contributions to the specific surface area from the mesopores and macropores are also analyzed as shown in Table 1. It is natural that the mesopores make major contributions to the specific surface area in all of the three HCl-washing samples. Furthermore, it can be seen that both the mesopores and macropores of the HCl-4h sample contribute less to the specific surface area as compared to those of the HCl-8h and HCl-16h samples. It suggests that the limited reduction time of 4 h influences the formation of both the mesopores and macropores in the HCl-washing samples.

In case of the HF-etching samples, the pore size distribution profiles obtained with the BJH method are similar for the reaction times of 4 h and 8 h, and slightly narrowed with the reduction time being extended to 16 h. The peak position of the pore diameter distribution profiles is around 33 nm, 50 nm, and 31 nm, respectively. Because mesoporous silica is totally removed by HF etching, the pore size distribution profiles of the HF etching samples are mainly determined by the pores within the silicon. With the reduction time extended from 4 h to 8 h, the conversion from silica to silicon is significantly enhanced. However, the

formation of silicon with a good structure control via a heating induced fusion process is not fully achieved, causing pores with larger size within the silicon. When the reduction time is further extended to 16 h, there is sufficient time allowing for the fusion process to reduce pore sizes within the silicon (from 50 nm to 31 nm). The average pore size derived from 4V/A is in the mesoscopic range between 12 nm and 21 nm. It indicates the existence of mesopores within the HF-etching silicon, which is consistent with nitrogen adsorption/desorption profiles. By combining information from the SEM and TEM images, it can be concluded that the "HF-etching" silicon is featured with a hierarchical macro-/mesoporous structure. The BET specific surface areas of the HF-etching silicon samples are continuously increased with extended reaction time (110.3 m^2g^{-1}, 118 m^2g^{-1}, and 134 m^2g^{-1}, respectively) due to an enhanced formation of mesopores. Nevertheless, the pore volume is gradually decreased with the reaction time changing from 4 h to 8 h and 16 h (0.57 cm^3g^{-1}, 0.45 cm^3g^{-1}, and 0.41 cm^3g^{-1}, respectively). The inverse decrease of the pore volume with increasing reduction time is possibly due to following reasons: Firstly, the HF treatment etches away silica and the mesopores within the silica particles are totally removed, which do contribute to the pore volume at all. Secondly, the pore diameters of the macropores decrease within the HF-etching samples along with an increased reduction time as proved by both, SEM and TEM. This decrease compromises the pore volume contribution coming from an increased reduction time. Thirdly, the slightly increased BET specific surface area indicates that the existence of the mesopores within the HF-etching samples is not enhanced that much with extended reduction. As a result, the increased pore volume from the mesopores cannot balance the diminished pore volume due to decreased diameters of the macropores, leading to a reduced total pore volume. Similar to the trend of HCl-washing samples, the contribution of the mesopores to the specific surface area in the HF-etching samples is increased with increased reduction time because of the enhanced formation of mesoporous structures. However, the contribution from the macropores increases firstly for the reduction times from 4 h to 8 h, followed by a decrease for the reduction time of 16 h. Because the diameters of the macropores decrease with increasing reduction time, it is reasonable that the macropores make less contribution to specific surface area for the reduction time of 16 h. As shown by the BJH pore size distribution profile in Figure 6, the peak position of the HF-8h sample is shifted to around

50 nm, indicating the portion of the pores with the diameter of larger than 50 nm is increased. This may help to enhance the contributions from the macropores towards overall specific surface area with the HF-8h sample.

By comparing the porosity between the HCl-washing and HF-etching samples, several conclusions can be drawn. Firstly, after HF etching, the specific surface areas of the samples for the reduction times of 8 h and 16 h are decreased because mesoporous silica particles are removed. Nevertheless, the 4 h sample exhibits a reverse trend, where the specific surface area is slightly increased after HF etching. Secondly, the formation of mesoporous silica is limited for the reduction time of 4 h, which indicates that the removal of the residual silica particles does not decrease the specific surface significantly. Thirdly, the un-reacted silica possesses high mass composition (49 %) in the whole sample, which is counted when gravimetric specific surface area is calculated. As a result, the mass portion of the un-reacted silica is excluded from the HF-etching sample, leading to an increased calculated specific surface area. Besides the specific surface area, the pore volumes of the samples for the reduction times of 8 h and 16 h are reduced after HF etching because of the removal of un-reacted silica. However, the pore volume of the HF-4h silicon is increased as compared to the HCl-4h sample because the mass of the un-reacted silica with limited porosity is excluded when the calculation is performed. The BJH pore size distribution profiles stay unchanged in the large size range independent of the reduction time, which is different from the HCl-washing samples. The mesoporous silica with small pore diameters produced by an increased reduction time is removed by HF etching. Therefore, the pore size distributions of the HF etching silicon are not shifted to a smaller size range with an increased reduction time. However, the average pore diameters of both the HCl-washing and HF-etching samples are in the mesoscopic range, indicating that the mesoporous structures are retained after HF etching. It implies that the mesopores not only exist in the un-reacted silica but also in the silicon. It is reasonable that the specific surface area contribution from the mesopores is decreased in the HF-etching samples for the reduction times of 4 h and 8 h. The slight increase of the specific surface area contribution from the mesopores within the 4 h reduction sample results from a removal of un-reacted silica. The macropores make more contributions to the specific surface areas after HF etching for the reduction times of 4 h and 8

h. However, it decreases at a reduction time of 16 h. The specific surface area contribution from the macropores is mainly determined by two reasons such as capability of the macropores to allow nitrogen adsorption/desorption and the size of the macropores. In the HCl-washing samples, the average diameters of the macropores are around 400 nm as indicated by the TEM images in Figure 4. After HF etching, the diameters of the macropores are decreased to 382±8 nm, 351±15 nm, and 332±12 nm, respectively. Even though the HCl-4h and HCl-8h samples possess macropores with larger diameters, the capability of the macropores to allow nitrogen adsorption/desorption may be limited. The interface between silica particles and surrounded porous silicon is not easily accessible due to limited conversion from silica to silicon (51 % and 58 %). In case of a reduction time of 16 h, the conversion yield is increased to 72 %, which is significantly higher than the samples with shorter reaction time. Along with an increased mass of silica reduced to silicon *in situ*, the boundary region between the silica particles and surrounding silicon is loose, which becomes easily accessible to nitrogen. As a result, the HF etching treatment significantly improves the accessibility of the macropores towards nitrogen adsorption/desorption in the samples for the reduction times of 4 h and 8 h, leading to enhanced specific surface area contribution. Regarding the sample after a reduction time of 16 h, it already possesses a high specific surface area contribution from the macropores in the HCl-washing sample because of the loose interface. Therefore, it does not make a significant contribution to improve the accessibility towards nitrogen gas when silica is removed. Instead, the macropores at the loose interface between the silica particles and surrounding silicon are eliminated after the HF etching treatment. The overall specific surface area contribution from the macropores is reduced in the sample for a reduction time of 16 h after HF etching.

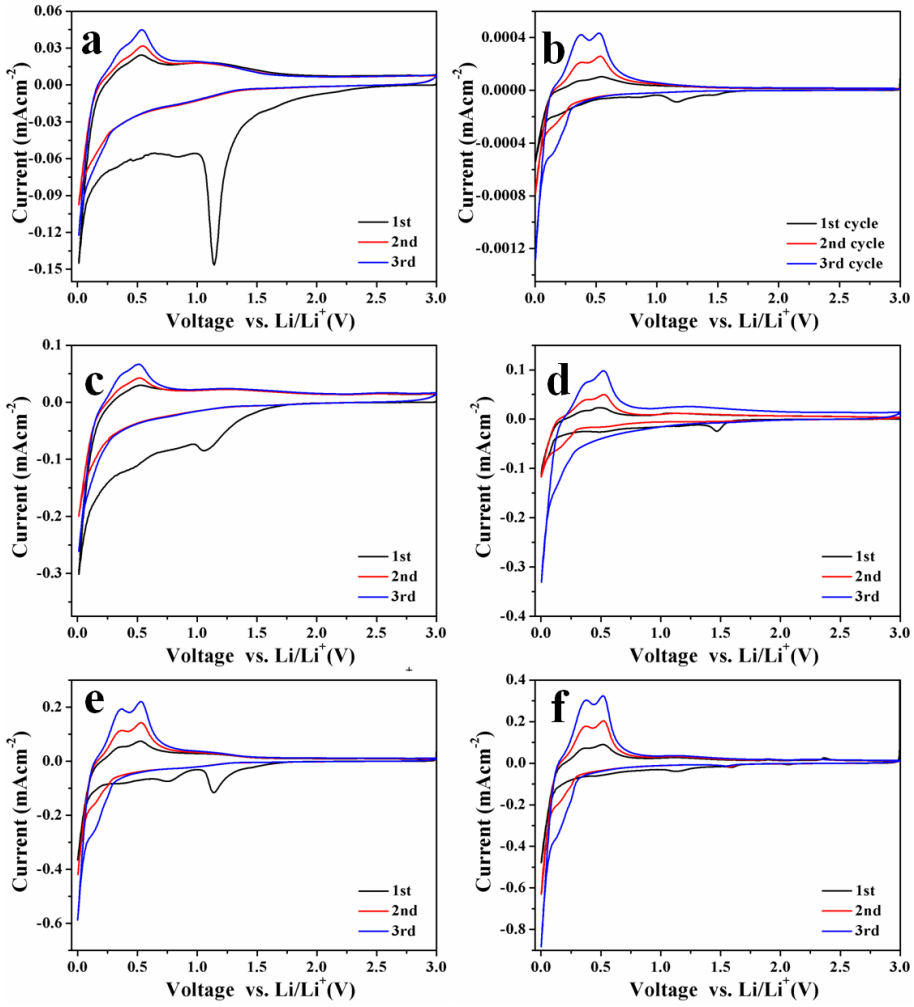

Figure S6. Cyclic voltammetry curves of porous silicon. (a)HCl-4h, (b) HF-4h, (c) HCl-8h, (d) HF-8h, (e) HCl-16h, and (f) HF-16h.

All the "HCl-washing" and "HF-etching" samples show characteristic CV peaks of the typical crystalline silicon. A broad reductive peak located at around 1.0 V - 1.5 V in the first lithiation scan is attributed to the formation of the SEI film. It is worth noticing that a strong peak originated from the SEI film is observed with the HCl-4h sample, which is different from other samples. Considering that the specific surface area of the HCl-4h sample is actually quite low as compared to the other samples, the strong peak originating from the formation of the SEI film in the first cycle is unlikely due to surface reactions, which are normally associated with high specific surface area. The limited reduction time of 4 hours may not be sufficiently long to reduce silica effectively, even though silicon is formed as confirmed by both the diffraction and imaging data. Instead, partial reduction of silica due to short reaction time may generate

silicon sub-oxide (SiO_x) species within the silica particles, which induces enhanced formation of the SEI film and inferior initial coulombic efficiency. [1] Besides the peak from the SEI film, a sharp reductive peak below 0.1 V is observed corresponding to the lithiation reaction of Si to form Li–Si alloy. While the other two oxidative peaks at around 0.35 V and 0.52 V in the delithiation scan are assigned to dealloying of the Li–Si alloys. The results are consistent with previously reported work. [2] In addition, all of the samples show an obvious peak intensity increase with increasing cycle numbers due to gradual infiltration of electrolyte into the porous Si electrodes. [3] The CV profiles of the HF-4h, HF-8h, HF-16h are quite similar to that of HCl-16h. It indicates that the HF etching process does not modify the fundamental lithiation/delithiation processes significantly as compared to the samples treated with HCl-washing only.

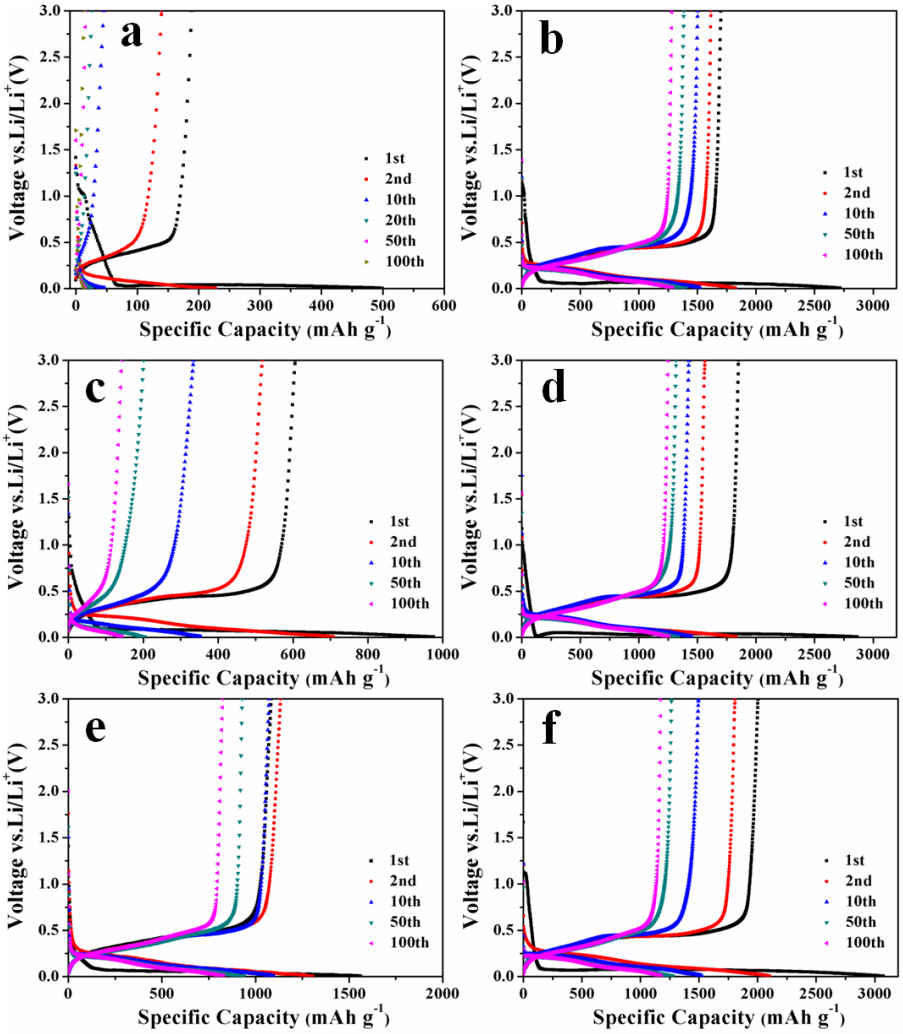

Figure S7. Galvanostatic discharge/charge profiles of porous silicon. (a) HCl-4h, (b) HF-4h, (c) HCl-8h, (d) HF-8h, (e) HCl-16h, and (f) HF-16h.

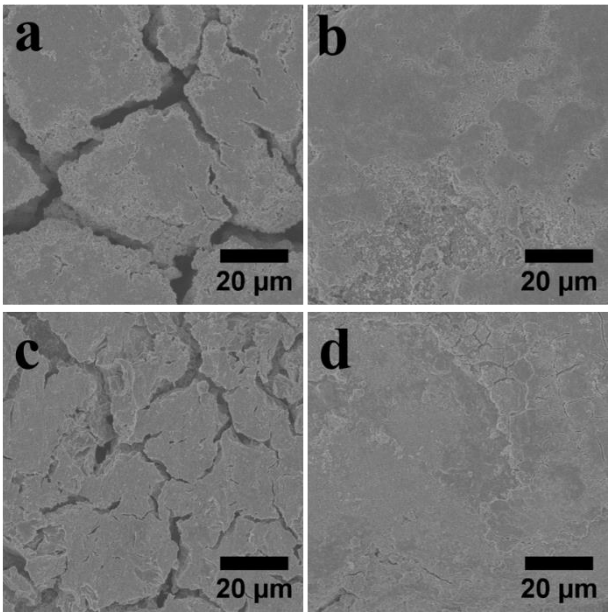

Figure S8. Top-view SEM images of the porous silicon electrodes after 100 discharge-charge cycles. (a) HCl-4h, (b) HF-4h, (c) HCl-16h, and (d) HF-16h.

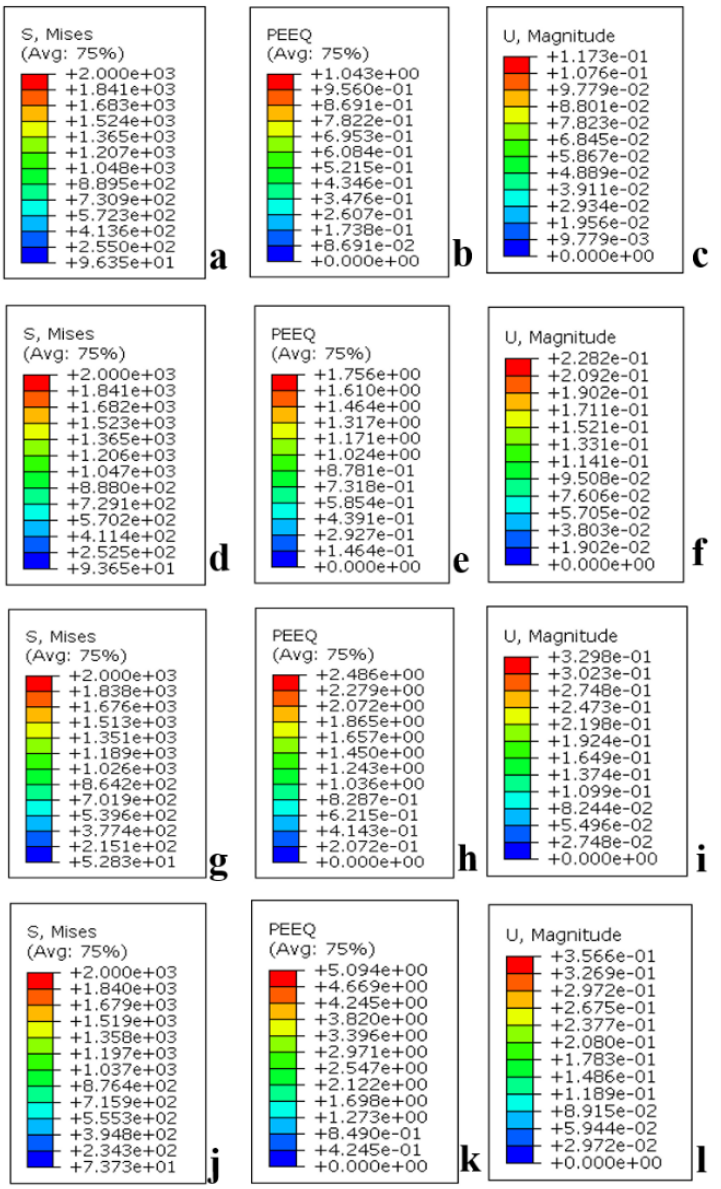

Figure S9. Magnified scalebars of Figure 7.

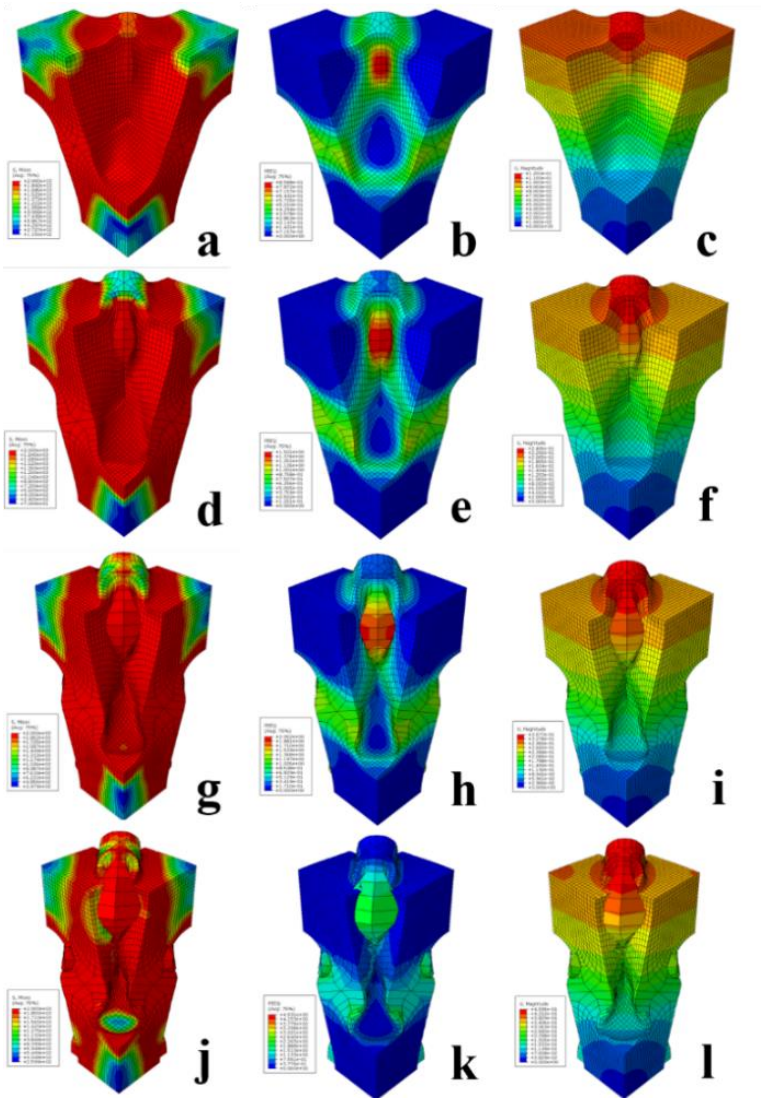

Figure S10. Stress (a, d, g, j), strain (b, e, h, k) and displacement (c, f, i, l) distribution of porous silicon calculated with the model structure III along with increasing volume change ratio. Details: 150 % (a, b, c), 200 % (d, e, f), 250 % (g, h, i), and 300 % (j, k, l).

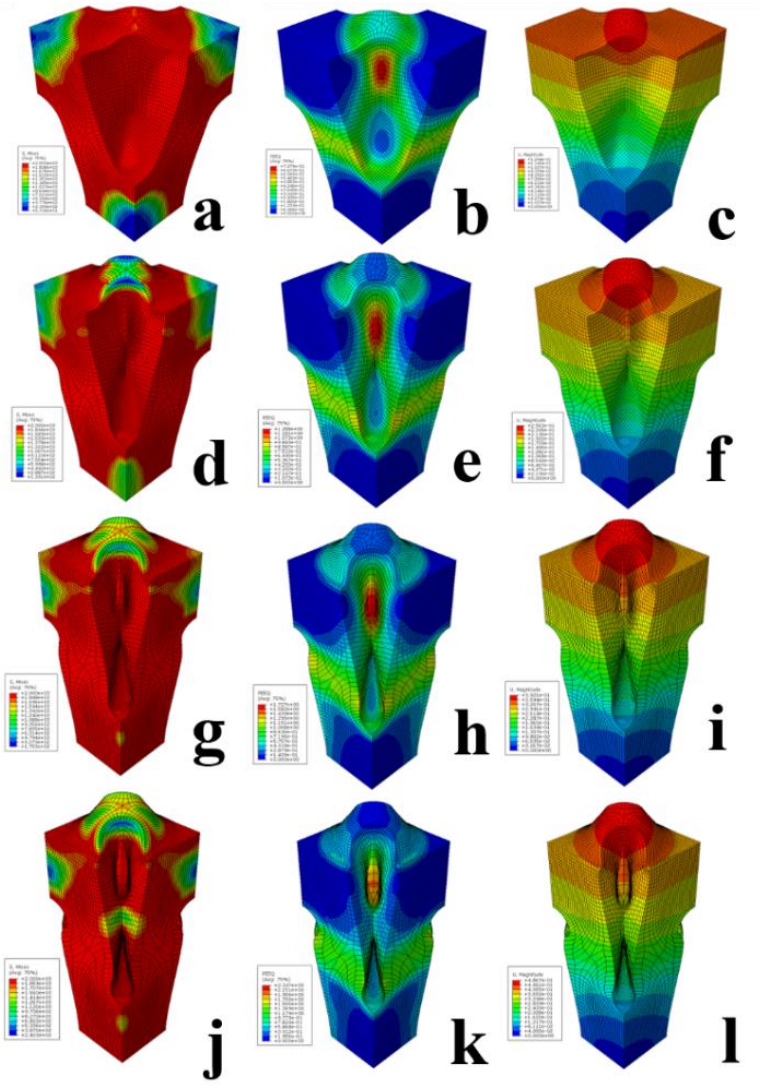

Figure S11. Stress (a, d, g, j), strain (b, e, h, k) and displacement (c, f, i, l) distribution of porous silicon calculated with the model structure IV along with increasing volume change ratio. Details: 150 % (a, b, c), 200 % (d, e, f), 250 % (g, h, i), and 300 % (j, k, l).

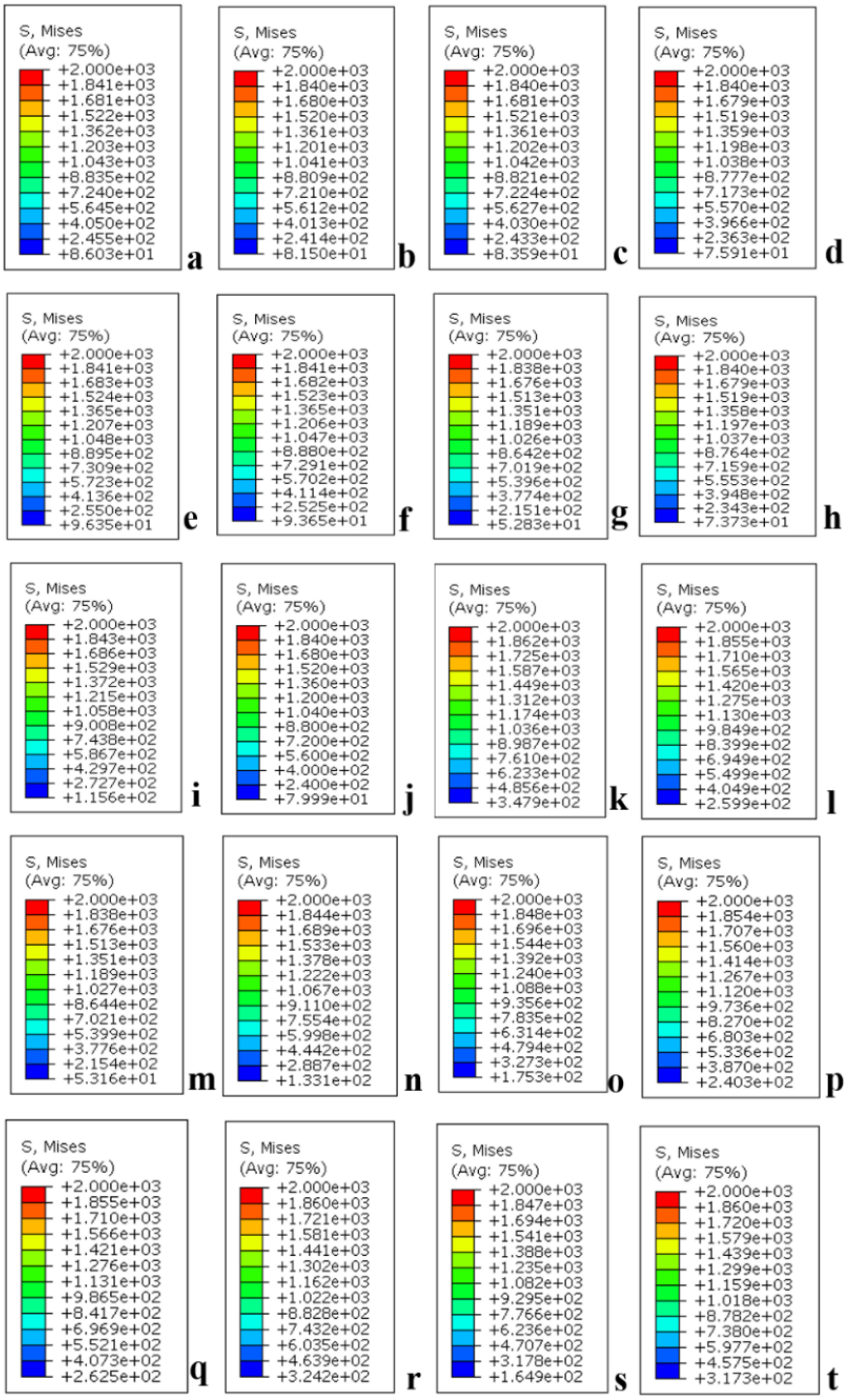

Figure S12. Magnified scalebars of Figure 8.

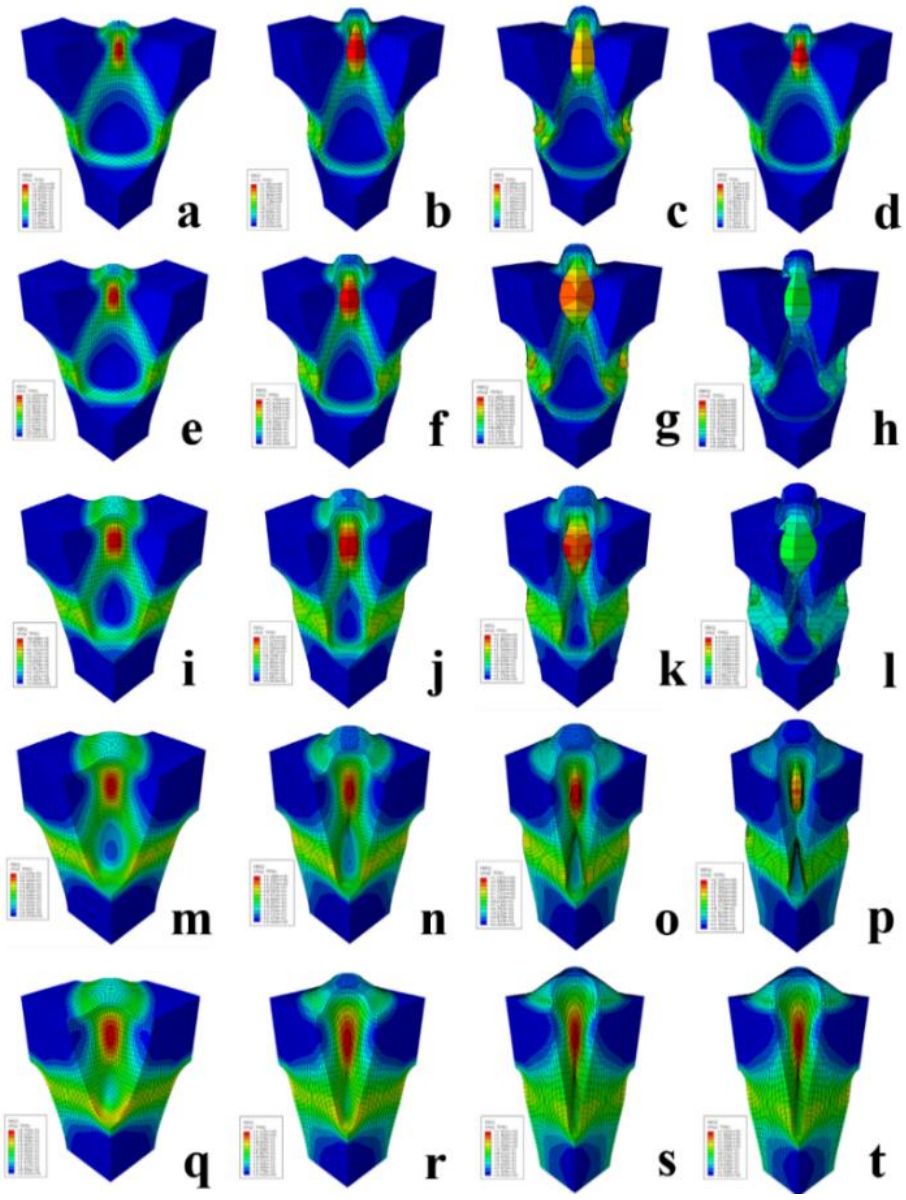

Figure S13. Strain distribution of porous silicon calculated with the model structure I (a, b, c, d), II (e, f, g, h), III (i, j, k, l), IV (m, n, o, p), V (q, r, s, t) along with increasing volume change ratio. Details: 150 % (a, e, i, m, q), 200 % (b, f, j, n, r), 250 % (c, g, k, o, s), and 300 % (d, h, l, p, t).

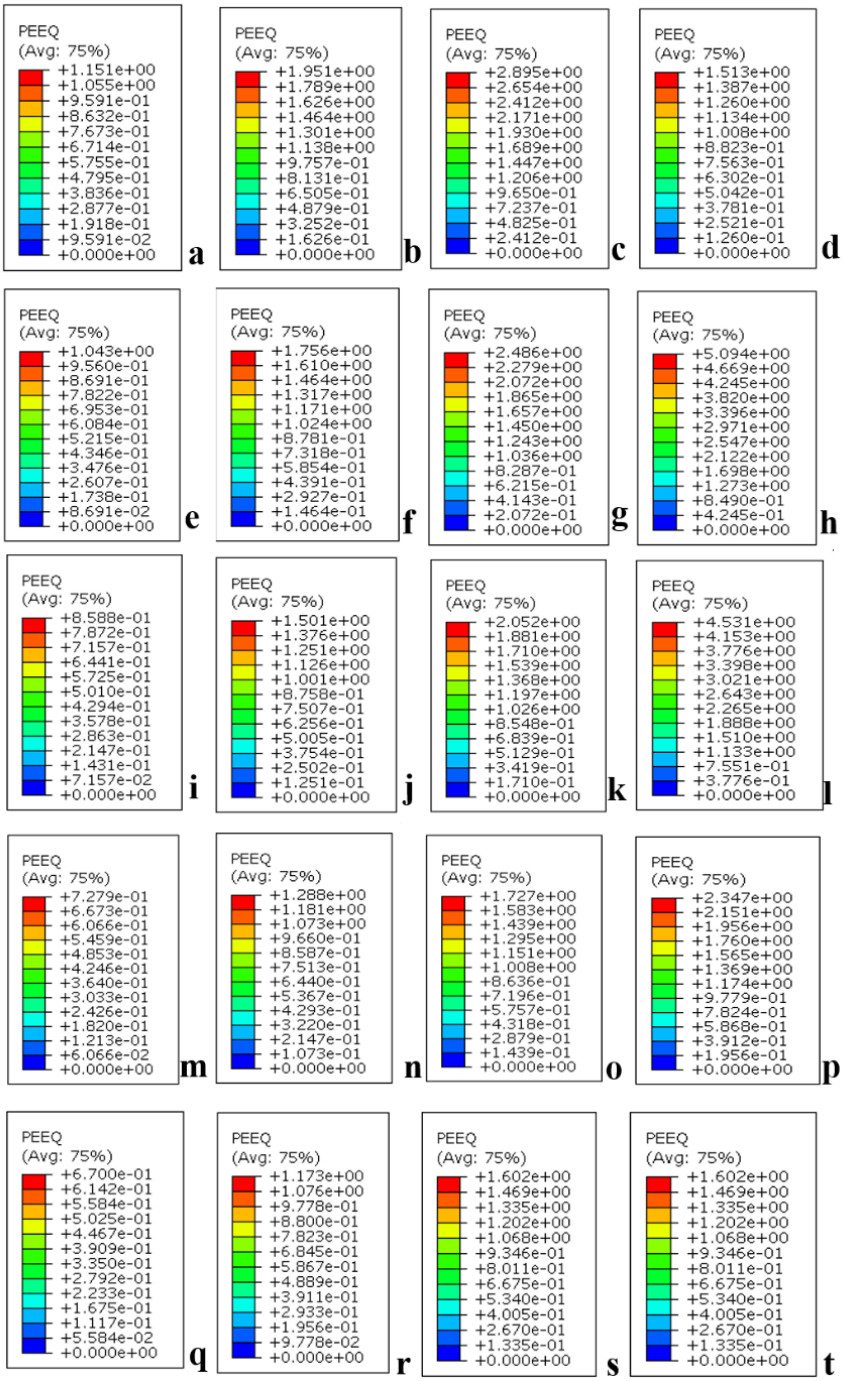

Figure S14. Magnified scalebars of Figure 9.

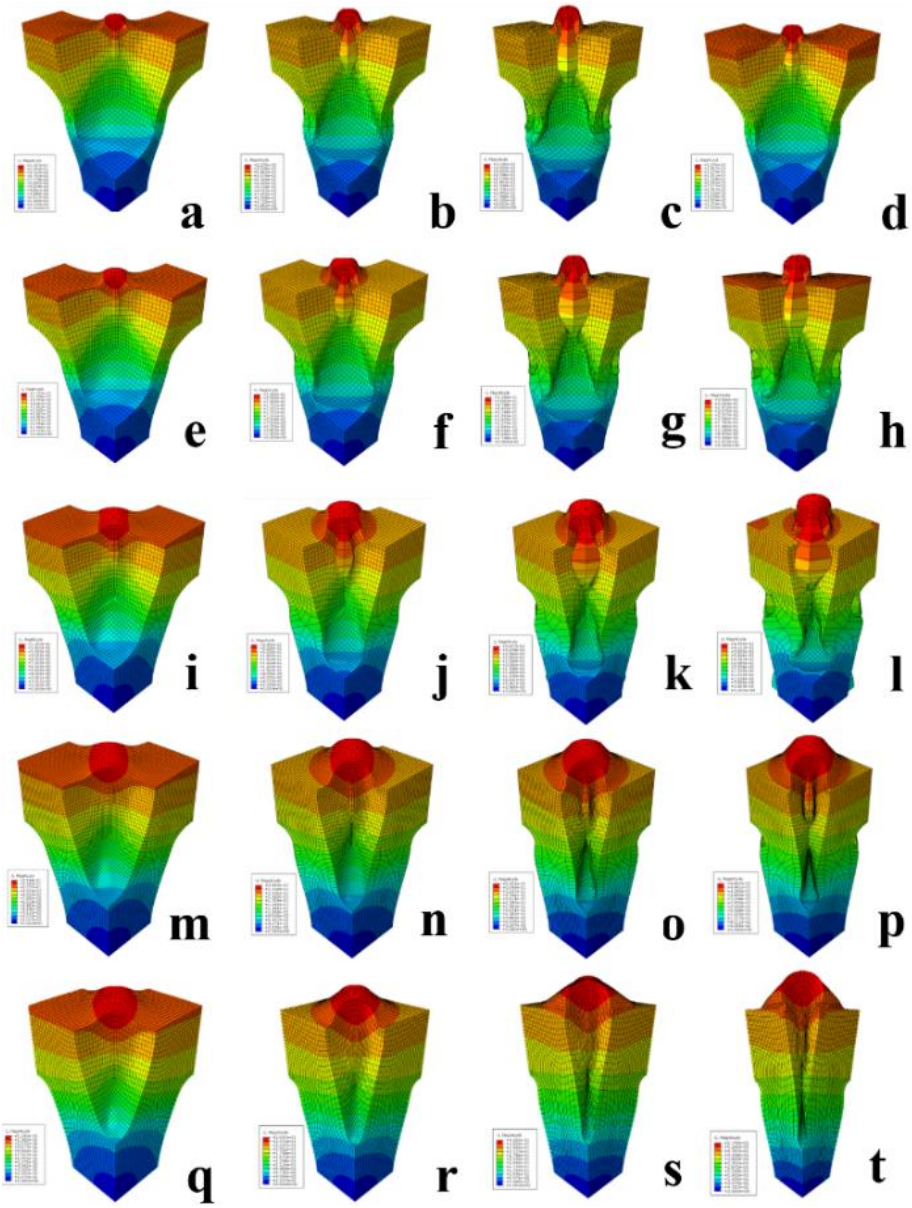

Figure S15. Displacement distribution of porous silicon calculated with the model structure I (a, b, c, d), II (e, f, g, h), III (i, j, k, l), IV (m, n, o, p), V (q, r, s, t) along with increasing volume change ratio. Details: 150 % (a, e, i, m, q), 200 % (b, f, j, n, r), 250 % (c, g, k, o, s), and 300 % (d, h, l, p, t).

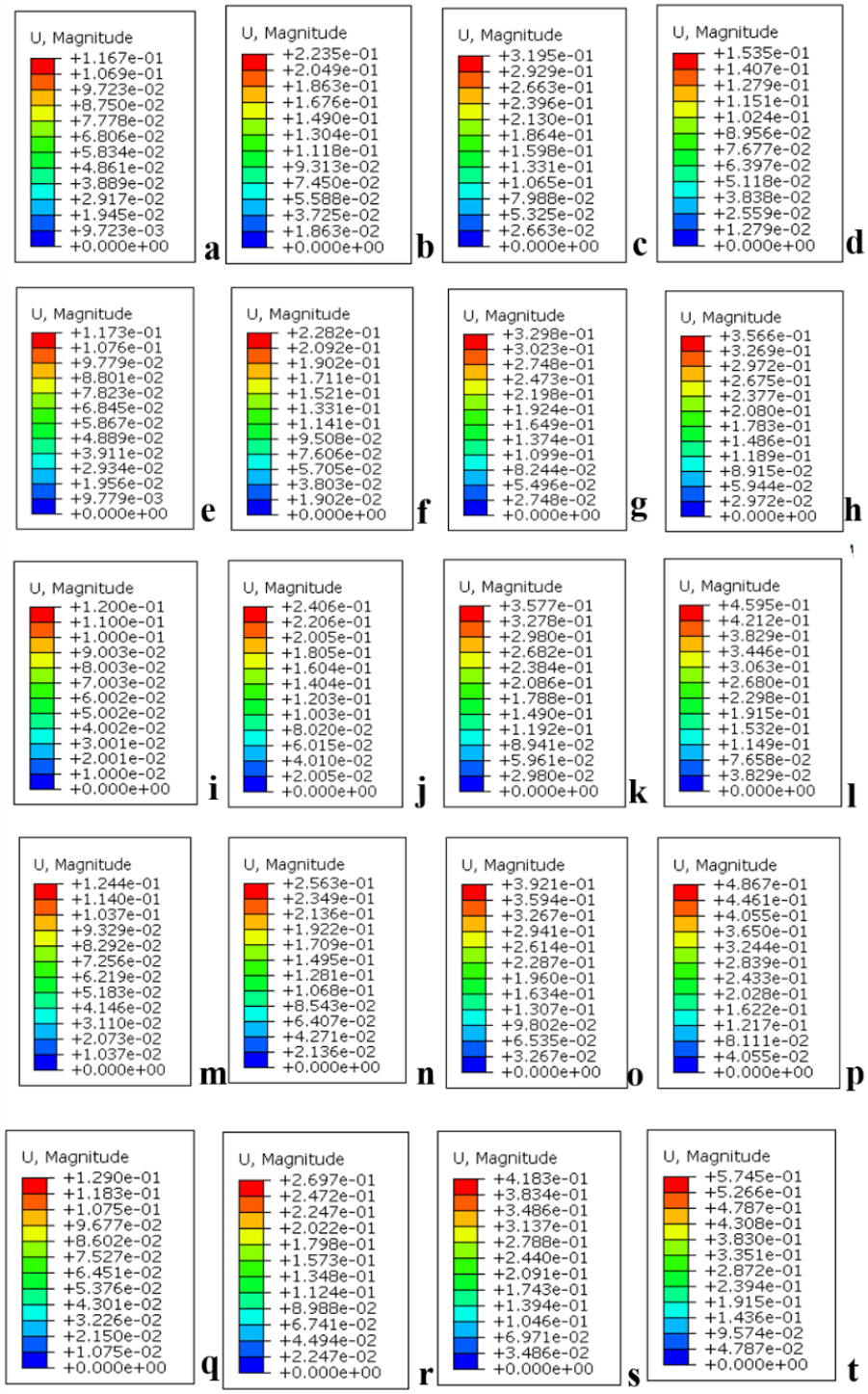

Figure S16. Magnified scalebars of Figure 10.

REFERENCES

1. Zhang, L.; Deng, J.; Liu, L.; Si, W.; Oswald, S.; Xi, L.; Kundu, M.; Ma, G.; Gemming, T.; Baunack, S.; Ding, F.; Yan, C.; Schmidt, O. G. Hierarchically Designed Siox/Sioy Bilayer Nanomembranes as Stable Anodes for Lithium Ion Batteries. *Adv. Mater.* **2014,** *26* (26), 4527-32.
2. Ju, Y.; Tang, J. A.; Zhu, K.; Meng, Y.; Wang, C.; Chen, G.; Wei, Y.; Gao, Y. Sio X /C Composite from Rice Husks as an Anode Material for Lithium-Ion Batteries. *Electrochim. Acta* **2016,** *191*, 411-416.
3. Zhang, J.; Zhang, C.; Liu, Z.; Zheng, J.; Zuo, Y.; Xue, C.; Li, C.; Cheng, B. High-Performance Ball-Milled Siox Anodes for Lithium Ion Batteries. *J. Power Sources* **2017,** *339*, 86-92.
4. Jia, H.; Zheng, J.; Song, J.; Luo, L.; Yi, R.; Estevez, L.; Zhao, W.; Patel, R.; Li, X.; Zhang, J.-G. A Novel Approach to Synthesize Micrometer-Sized Porous Silicon as a High Performance Anode for Lithium-Ion Batteries. *Nano Energy* **2018,** *50*, 589-597.
5. Zhou, X.; Wu, L.; Yang, J.; Tang, J.; Xi, L.; Wang, B. Synthesis of Nano-Sized Silicon from Natural Halloysite Clay and Its High Performance as Anode for Lithium-Ion Batteries. *J. Power Sources* **2016,** *324*, 33-40.
6. Wang, B.; Li, X. L.; Luo, B.; Jia, Y. Y.; Zhi, L. J. One-Dimensional/Two-Dimensional Hybridization for Self-Supported Binder-Free Silicon-Based Lithium Ion Battery Anodes. *Nanoscale* **2013,** *5* (4), 1470-1474.
7. Hu, R.; Sun, W.; Chen, Y.; Zeng, M.; Zhu, M. Silicon/Graphene Based Nanocomposite Anode: Large-Scale Production and Stable High Capacity for Lithium Ion Batteries. *J. Mater. Chem. A* **2014,** *2* (24), 9118.
8. Tian, H.; Tan, X.; Xin, F.; Wang, C.; Han, W. Micro-Sized Nano-Porous Si/C Anodes for Lithium Ion Batteries. *Nano Energy* **2015,** *11* (0), 490-499.